Available online at www.sciencedirect.com
ScienceDirect
Journal of Photochemistry and Photobiology A: Chemistry 195 (2008) 10–22
Journal of Photochemistry and Photobiology A:Chemistry
www.elsevier.com/locate/jphotochem

A directly-dissociative stepwise reaction mechanism for gas-phase peroxyacetic acid

B.K. Keller*, M.D. Wojcik[1], T.R. Fletcher

University of Idaho, Department of Chemistry, P.O. Box 442343, Moscow, ID 83844-2343, United States

Received 19 June 2007; received in revised form 29 August 2007; accepted 3 September 2007
Available online 6 September 2007

Abstract

The dissociation of peroxyacetic acid (PAA, $CH_3C(O)OOH$) was studied by UV laser photolysis in the gas phase under collision-free conditions. Three pathways are proposed for PAA dissociation that ultimately produce $CH_3 + CO_2 + OH$. Two pathways are stepwise with sequential bond dissociation and the other pathway is concerted with simultaneous fission of the same bonds. The laser-induced fluorescence (LIF) spectrum of OH was analyzed after 266 and 240 nm photolysis of PAA. OH is produced in the $^2\Pi$ ground electronic state with no vibrational energy ($v'' = 0$) and rotational distributions that peak at $N'' \approx 3$–4 and extend to $N'' = 11$ at both photolysis wavelengths. Spin-orbit population ratios of the ground electronic state were slightly above unity for both studies. The average OH Λ-doublet ratio was 1.07 ± 0.14 after 266 nm photolysis, which indicates that OH is produced by torsional forces. At 240 nm PAA photolysis, the Λ-doublet ratio increased from unity at $N'' = 4$ to a statistical value of $\sim$2 at $N'' = 11$. Average OH translational energies determined from Doppler profiles were 34 ± 2 and 43 ± 2 kcal mol^{-1} at 266 and 240 nm photolysis, respectively. The average speed of OH is used to determine the total translational energy of products for the proposed stepwise and concerted pathways. The calculated total translational energies are compared to thermochemical available energy calculations for each pathway to determine the viability of the reactions. Experimental results indicate that dissociation occurs from an excited state, so a comparison of 266 and 240 nm photolysis data is made to discover the direct versus indirect nature of the mechanism. The UV spectra of PAA, acetic acid, hydrogen peroxide, and methylhydroperoxide are reviewed in light of the results. This study concludes that PAA photolysis occurs through initial stepwise O–O bond dissociation by a directly-dissociative mechanism from a highly-repulsive electronic state like the hydroperoxides and an indirect mechanism from an exit channel barrier similar to acetic acid is not accessed at these wavelengths.

Keywords: Peroxy acids; Peracids; Photodissociation; Laser-induced fluorescence

1. Introduction

This study investigates the possible photofragmentation pathways of a peroxy acid. The peroxycarboxylic acids, named "peroxy" or "per" acids have the general formula, RC(O)OOH. Peroxyformic acid, HC(O)OOH, is the simplest peracid but is highly unstable [1]. Peroxyacetic acid, $CH_3C(O)OOH$ or PAA, is often preferred for physical studies of this class of compound because it is more stable. Peroxy acids in the liquid and vapor phase exist solely as intramolecularly-hydrogen bonded monomeric species unlike carboxylic acids, which have monomer-dimer equilibrium in the gas phase [2]. Many of the observed physical properties of peroxy acids that distinguish them from their similar carboxylic acids can be attributed to intramolecular hydrogen bonding [3]. PAA has a lower boiling point (110 °C) than acetic acid (118 °C) [4]. Likewise, the melting point of PAA (0.2 °C) is lower than acetic acid (16.7 °C). Intramolecular hydrogen bonding in peroxy acids also makes them weaker acids than carboxylic acids. Early investigations of the conformation of peroxy acids suggested a folded five-membered ring with a dihedral angle of 72° [5]. Microwave spectra of peroxyformic acid and PAA showed strong evidence for a planar structure [6,7]. Calculations at the ab initio MO level also indicated that an intramolecular hydrogen bonded *cis*-planar ring structure was the most stable conformation [8].

Photodissociation of PAA may follow one or more of three possible pathways: two stepwise and one concerted as shown in reactions (R1–R3). The first stepwise reaction (R1) is initiated by homolytic O–O bond cleavage, the weakest bond in the

* Corresponding author.
E-mail address: wavenumber9@hotmail.com (B.K. Keller).
[1] Current address: Pacific Northwest National Laboratory, P.O. Box 999, K5-25 Richland, WA 99352, United States.

1010-6030/$ – see front matter © 2007 Published by Elsevier B.V.
doi:10.1016/j.jphotochem.2007.09.001

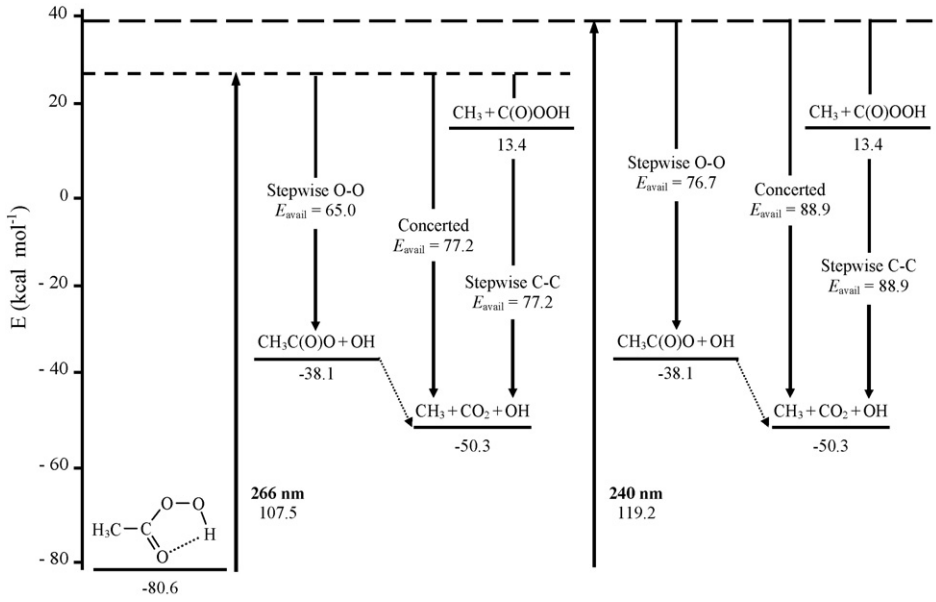

Fig. 1. Available energy (E_{avail}) calculations for PAA photodissociation at 266 and 240 nm along three proposed pathways, two stepwise and one concerted (R1–R3). All energy values are in kcal mol^{-1}. See text for details concerning the calculations.

molecule, to generate two photoproducts. Secondary decomposition of the acetyloxy radical, $CH_3C(O)O$, ultimately produces the three final reaction products. Reaction R2 follows a concerted mechanism with simultaneous fission of O–O and C–C bonds. Reaction R3 is also stepwise but instead begins with C–C bond cleavage, which is much stronger than the O–O bond and may be followed by secondary decomposition of C(O)OOH.

$$CH_3C(O)OOH \rightarrow CH_3C(O)O + OH$$
$$\rightarrow CH_3 + CO_2 + OH\,(\text{secondary}) \quad (R1)$$

$$CH_3C(O)OOH \rightarrow CH_3 + CO_2 + OH \quad (R2)$$

$$CH_3C(O)OOH \rightarrow CH_3 + C(O)OOH$$
$$\rightarrow CH_3 + CO_2 + OH\,(\text{secondary}) \quad (R3)$$

The heats of formation and bond strengths in PAA and its dissociation products are not known exactly. Heats of formation presented here were estimated using group additivity methods, which can be accurate within 1–2 kcal mol^{-1} for many organic compounds [9]. The heat of formation determined for PAA is −80.6 kcal mol^{-1} where the O–O bond dissociation energy is 42.5 kcal mol^{-1}. These two values are used to determine the available energies (E_{avail}) where OH is produced in Fig. 1 for reaction pathways (R1–R3). Photolysis at 266 nm deposits 107.5 kcal mol^{-1} of excitation energy into the molecule. The stepwise O–O pathway has E_{avail} = 65 kcal mol^{-1} for the two products. The concerted pathway leaves E_{avail} = 77.2 kcal mol^{-1} for three products. The stepwise C–C pathway also has E_{avail} = 77.2 kcal mol^{-1} but only after secondary C(O)OOH decomposition, which produces CO_2 and OH. Secondary decomposition is also the major source of E_{avail} in this pathway. The heat of formation of C(O)OOH was determined by subtracting the methyl radical heat of formation from that of PAA and adding 94 kcal mol^{-1} for the C–C bond strength [10]. Available energy calculations for reactions R1–R3 at 240 nm photolysis, which deposits 119.2 kcal mol^{-1} of excitation energy into PAA, are shown on the right side of Fig. 1. The stepwise O–O pathway now has E_{avail} = 76.7 kcal mol^{-1}, while the concerted and the stepwise C–C pathways both have E_{avail} = 88.9 kcal mol^{-1}. It is important to note that other calculation methods indicate a heat of formation of PAA around −76 kcal mol^{-1} [11], and some estimates place the O–O bond dissociation energy as high as 48 kcal mol^{-1} [12,13]. The heat of formation of PAA and its photoproducts in Fig. 1 may vary by more than 1–2 kcal mol^{-1}, but this should have little effect upon the relative available energies between the stepwise and concerted pathways.

The impetus for investigating gas-phase peroxy acid dissociation comes from previous thermolysis and photolysis studies of peroxy acids and the closely related peroxy esters. The decomposition rates of peroxy esters are believed to be dependent upon the acyl product stability and both stepwise and concerted decomposition pathways are reported for these compounds [14,15].

Vapor-phase thermolysis of PAA in toluene carrier gas indicated two simultaneous decomposition reactions [16]. The first reaction was homolytic O–O bond cleavage (R1) with an estimated bond dissociation energy of 30–34 kcal mol^{-1} followed by loss of carbon dioxide from acetyloxy radical. A second heterogeneous reaction where PAA loses oxygen to form acetic acid occurred on the glass walls of the reaction vessel. Solution-phase thermal decomposition of PAA in aromatic solvents also had two competing reactions [17]. Homolytic O–O bond dissociation and a second reaction through an oxygenated intermediate that lead to formation of acetic acid

and phenol compounds were expected. The homolytic bond dissociation energy of 31.5–33.0 kcal mol^{-1} was in agreement with the vapor phase study [16] but both estimations are lower than more recently reported values [12,13].

Photolysis studies of peroxy acids are few and many are limited to energy transfer from photo-excited aromatic solvents to the peroxy acid. Photo-induced decomposition of PAA was studied in a variety of alkyl aromatic solvents [18–21]. A Hg lamp was the light source in these studies but quartz and pyrex filters allowed passage of specific portions of the lamp spectrum (253.7 nm majority and >290 nm excitation, respectively). Light at 253.7 nm excited the aromatic solvent that transfers energy to the peracid, which is not so relevant to our study. However, excitation at >290 nm was predominantly absorbed by PAA (peroxy acids absorb light to 300 nm where the alkylbenzene solvents do not). These studies indicated that O–O bond homolysis in PAA largely produced hydroxylated alkyl side-chain aromatic products. UV photolysis of PAA in cyclohexane likewise yielded mostly cyclohexanol [22].

To the best of our knowledge there have been no photochemical studies of peroxy acid dissociation in the gas phase under collision-free conditions. Our gas phase photodissociation study of PAA has many advantages over previous investigations. Low sample pressures (mTorr) and short time scales (nanoseconds) allow measurement of dissociation products before collisional relaxation occurs. Laser excitation also deposits a very specific amount of energy directly into the peroxy acid to promote dissociation. The photochemistry of PAA will be compared to gas phase studies of other related molecules. Relevant here are the carboxylic acids and hydroperoxides. The photodissociation dynamics of PAA may be similar to the hydroperoxides or it may be more like the carboxylic acids. The dynamics may also be entirely unique to the peroxy acid group.

Initial results from PAA photodissociation at 266 nm clearly indicated that dissociation likely occurs from an excited electronic state. Photolyzing a molecule at multiple wavelengths within the same electronic absorption band can provide more detailed information about the dissociation dynamics than a single wavelength study. A good example of this comes from gas phase studies of acetic acid photodissociation at 218 and 200 nm [23,24]. The reaction thermochemistry and kinetic energy analysis of products were used to demonstrate that acetic acid undergoes indirect dissociation after C–O bond breakage where the OH product translational energy was generated from an exit channel barrier. The direct or indirect nature of excited state dissociation of PAA is investigated in a manner similar to acetic acid by comparing product energies at 266 and 240 nm. The difference in the photolysis wavelengths results in an 11.6 kcal mol^{-1} increase in the excitation energy. How the added excitation energy is partitioned, whether it goes into translation or internal excitation of products will reveal whether the dissociation process is direct or indirect. The direct process occurs from a repulsive excited electronic state and will produce similar partitioning of the available energy into internal and translational excitation of products at both 266 and 240 nm photolysis. The indirect mechanism occurs on a surface with an exit channel barrier where the barrier height is the source of translational excitation as occurs in acetic acid [23,24] and acetone [25]. A comparison of the product energy distributions at each photolysis wavelength will show a decrease in the translational energy partitioning if the indirect process occurs.

This work has three main goals. The first is to determine the primary photodissociation pathway for PAA, is photodissociation stepwise or concerted? The second goal is to determine the nature of the reaction pathway, is dissociation direct or indirect? Later reports will address the third goal, which is to demonstrate the extent of control that can be exerted in this class of compound to ultimately attempt to manipulate the branching ratio between stepwise and concerted reaction pathways.

2. Experimental/materials and methods

2.1. Synthesis and analysis of PAA sample solutions

To achieve the concentration and purity necessary for these experiments we chose to synthesize PAA in the laboratory by the method of Krimm [26] using 50% H_2O_2. The reaction yield was 75% in conversion of acetic acid to PAA. H_2O_2 and acetic acid were removed by vacuum distillation at 15 Torr through a 40 cm vigreux column with a 22–26 °C boiling point at the column head and a pot temperature <55 °C. Residual H_2O_2 was measured by cerium(IV) sulfate titration then the PAA concentration was determined iodometrically [27]. A separate NaOH titration using thymolpthalien indicator (PAA $pK_a = 8.2$) gave the total amount of acid (PAA and acetic acid) in the solution. The total acid minus the amount of PAA gave the amount of acetic acid. Sample composition was 92 wt% PAA, <1 wt% acetic acid, <0.02 wt% H_2O_2, and the remainder was water. PAA solutions were stored at 5 °C and were degassed and analyzed before use.

2.2. OH LIF apparatus

The OH photofragment laser-induced fluorescence (LIF) spectrum was measured after UV laser photolysis of PAA. The main components of the LIF apparatus in Fig. 2 are the pump and probe laser sources; the sample chamber and vacuum components; the collection optics, PMT, and signal amplifiers; and the instrumental control and data storage devices. The pump and probe beams passed through the sample chamber in a parallel counter-propagating manner. The pump laser initiated photolysis of PAA in the reaction cell, which was followed by LIF interrogation of the OH $A^2\Sigma^+ - X^2\Pi$ transitions with the probe laser. The 266 nm photolysis beam was obtained from a Nd:YAG laser (Spectra-Physics, GCR-11) operating on the fourth harmonic (10 Hz, 15 ns pulse width, vertical polarization) that produced 15 mJ $pulse^{-1}$. The 240 nm photolysis beam was generated by Raman shifting (1st anti-Stokes with 1 mJ $pulse^{-1}$) the 266 nm beam within a 1 m stainless steel tube filled with 20 psi of hydrogen [28,29]. A second Nd:YAG laser (Spectra-Physics, DCR-11) operating on the second harmonic (532 nm, 10 Hz,

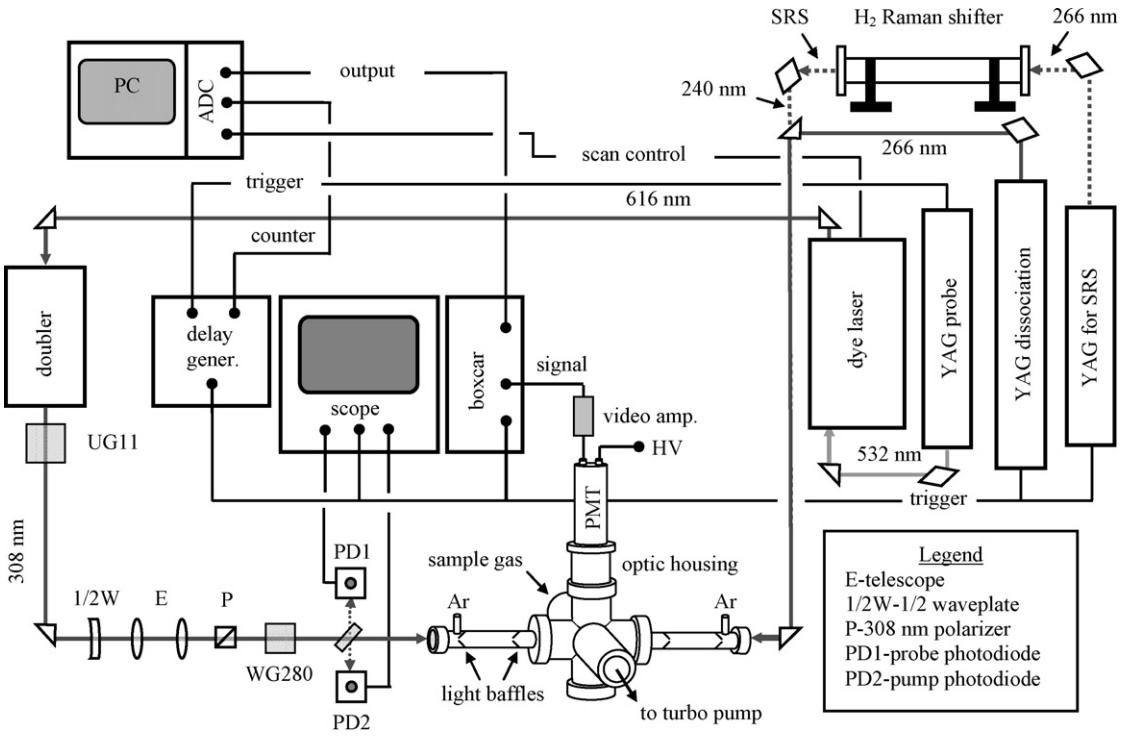

Fig. 2. Experimental apparatus used to measure the OH LIF spectrum after UV laser photolysis of PAA. The Raman shifter at the upper right generates the 240 nm photolysis beam.

8 ns pulsewidth, 80 mJ pulse^{-1}) pumped a dye laser (Lumonics HD-300B) using a 50/50 mixture of R640 and DCM to produce tunable light from 612 to 624 nm. The dye laser output was frequency doubled in a KDP crystal (Inrad Autotracker II) to make a tunable probe beam from 306 to 312 nm. A colored glass filter (Schott UG-11) was used to separate the LIF probe beam from the visible fundamental. A 3× expanding telescope decreased the UV probe beam fluence and a polarizing beamsplitter cube and ½ waveplate allowed for polarization adjustment and energy maintenance. Another filter (Schott WG-280) blocked photolysis light from entering the probe beam optics. A CaF_2 window in the beam pathways allowed for sampling of both laser beams with photodiodes to correct the LIF signal for power fluctuations.

The gas sample chamber was of stainless steel construction with two arms with baffles to reduce scattered light from both beams. The pressure of PAA was maintained at 20 mTorr, which was admitted directly into the chamber. An additional 40 mTorr of Ar (Oxarc, 99.995%) buffer was applied as needed through ports behind the fused silica windows to prevent deposit buildup after long-term UV irradiation. A turbomolecular pump evacuated the chamber and the pressure was monitored with a capacitance manometer. LIF from OH was collected using two CaF_2 lenses (f/2) through a 3 mm slit. Glass filters (UG1, WG280) and an interference filter (Melles-Griot, 310 ± 10 nm at 16° mount angle) were used to block scattered photolysis beam light. OH LIF fluorescence was detected with a PMT (Hamamatsu 943-02). The PMT signal was amplified with a DC-100 MHz video amplifier and sent to a boxcar integrator (Stanford Research SR250) using a 1.5 μs collection gate. Thirty laser shots were averaged for each data point in the LIF spectrum (Fig. 3). 100-shot averaging was used for Doppler profile analyses (Fig. 7). The signals were sent to a 16-bit analog-to-digital converter (National Instruments) interfaced to a PC running Labview software. A delay generator (Stanford Research DG535) controlled all the experimental timing. A delay time of 100 ns was used between the pump and probe beams.

2.3. Probe beam saturation studies

In the absence of saturation the LIF signal is directly proportional to the lower level population in the probed transition [30] but OH LIF transitions are easily saturated at elevated laser intensities. Saturation refers to the nonlinear behavior of the LIF signal intensity that can be avoided at low laser power [31]. Two methods were used to confirm that LIF signals were not saturated. The first method was to measure the signal dependence upon the probe beam fluence. This was done for both Q_14 and R_14 OH lines because they are the first to saturate. The Q_14 transition was linear with probe laser fluence below 30 μJ cm^{-2} and the R_14 line below 60 μJ cm^{-2}. The second saturation test was to compare the Q_14 line intensity with that of the Q_14' satellite as a function of the probe beam fluence [32]. Q and Q'-branch transitions probe the same initial population, so in the absence of saturation the signal intensity ratio should equal the ratio from the Einstein B-factors. The Q_14 to Q_14' signal ratio was similar to the B-factor ratio at fluences below 30 μJ cm^{-2}. At higher fluence levels, the Q_14 signal began to saturate and the Q_14 to Q_14' signal ratio decreased. For the OH rotational spectra, the probe beam fluence was kept well below the Q-branch saturation level at 1 μJ pulse^{-1} with 3 mm beam diameter. R-branch Doppler profiles were measured at 3 μJ pulse^{-1} to obtain a greater signal-to-noise ratio.

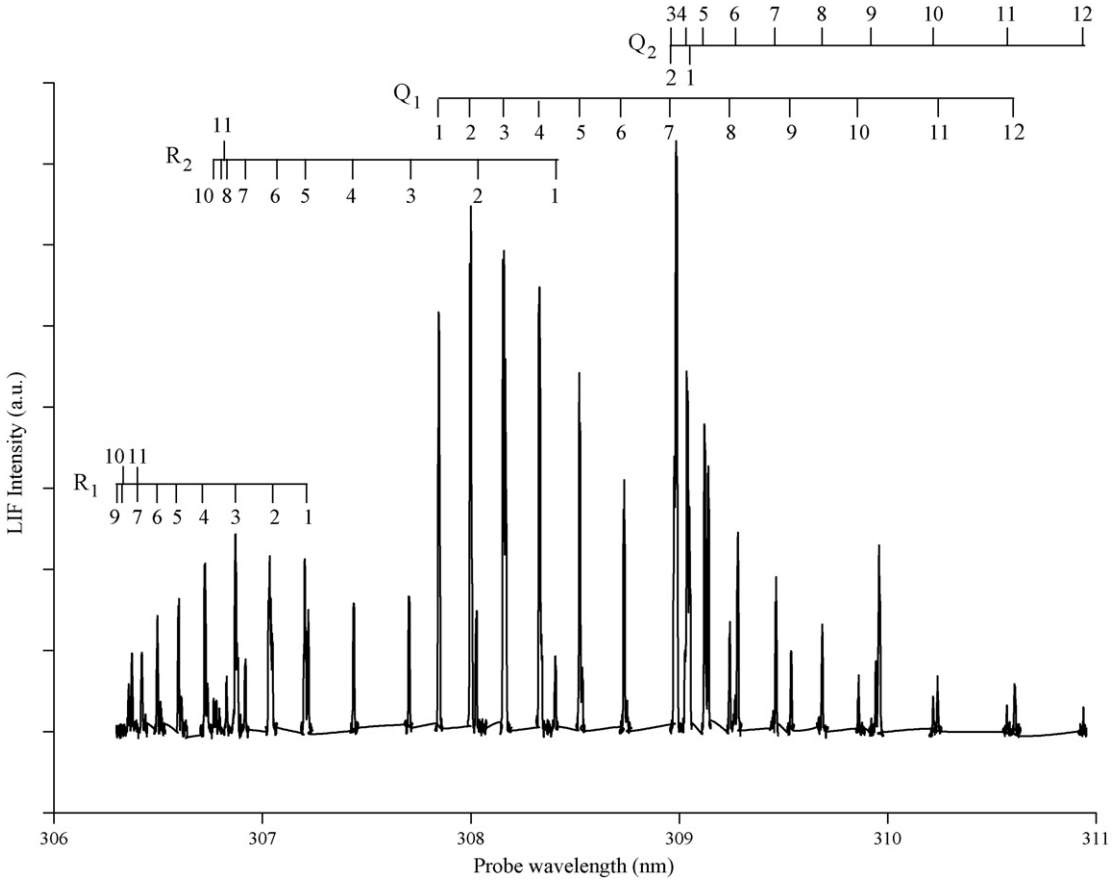

Fig. 3. OH $A^2\Sigma^+ - X\,^2\Pi$ (0-0) LIF spectrum from PAA dissociation at 266 nm.

3. Theory and calculations

3.1. OH radical spectroscopy

OH radical has a large rotational constant and is easily probed by LIF detection. The spectroscopy of OH is well known and the molecular constants and term values have been well characterized [33]. The spectrum of the OH $A^2\Sigma^+(v''=0) - X\,^2\Pi_{3/2,1/2}$ $(v''=0)$ transitions in the 300–320 nm region were assigned according to Dieke and Crosswhite [34]. Diagrams showing the $A^2\Sigma^+ - X\,^2\Pi$ branch transitions and selection rules are available elsewhere [35,36]. The $^2\Pi$ ground electronic state vibrational and rotational quantum numbers are designated v'' and N''. Angular momentum coupling splits the $^2\Pi$ ground state into f_1 and f_2 ($^2\Pi_{3/2}$ and $^2\Pi_{1/2}$) spin-orbit states. Λ-doubling further splits each spin-orbit state. The Q and R-branches include all the populations in the ground electronic state and thus provide the full OH quantum state distribution.

3.2. OH collision factor

The average translational energy of OH products from PAA dissociation was obtained by Doppler spectroscopy. OH reaction products are generated with high velocities and may lose a portion of their initial translational energy via collisions with parent or buffer gases (PAA or Ar). Collisional relaxation results in narrowing of the Doppler linewidth that correspondingly decreases the product translational energy, which ultimately may result in misinterpretation of the major reaction pathway. Ar buffer gas was not used in the Doppler profile analysis to minimize the effects of collisional relaxation. The OH product collision rate is proportional to the relative speed of OH and PAA and also to their molecular sizes. The number of collisions per unit time, Z, that OH will experience with PAA is approximated in Eq. (1) [37].

$$Z = \pi\, b_{\max}^2 v_r\, n_{\mathrm{PAA}}* \tag{1}$$

The collisional impact parameter $b_{\max}$ is the sum of the hard-sphere molecular radii, v_r is the center of mass (COM) velocity of OH relative to PAA, and $n_{\mathrm{PAA}}*$ is the number density of PAA molecules. The radius of OH is 0.97 Å [38] and the estimated radius for PAA is 2.2 Å [11]. The maximum impact parameter between the two molecules is $b_{\max} = 3.2$ Å. The average COM velocity of OH from a typical experiment at 266 nm is 4100 m s^{-1} and the average velocity of PAA under thermal conditions is 300 m s^{-1}, which gives a relative velocity, v_r, of 4110 m s^{-1}. At 20 mTorr, $n_{\mathrm{PAA}}*$ is 6.43×10^{20} molecule m^{-3}. This gives a collision rate of $Z = 8.5 \times 10^5$ collisions s^{-1}. With a 100 ns time delay between pump and probe lasers, the average OH product experienced ~0.085 collisions before LIF measurement. Further decreasing the pump-probe delay did not change

the Doppler linewidth, which confirmed that OH was measured collision-free.

3.3. Doppler profile analysis to determine OH translational energy

The average OH translational energies were determined by Doppler spectroscopy. The OH fragment LIF spectral lines are Doppler-broadened due to the velocity of the product relative to the probe beam propagation vector. Doppler profiles were measured by scanning the probe laser using a small scanning step size (0.0002 nm). The $R_2 8$ feature (Fig. 7) was chosen to determine the average OH translational energy. Assuming an isotropic distribution of OH velocity vectors, the data were fit with a Gaussian function which includes the experimental nascent OH linewidth, $\Delta\nu_{expnas}$, with a full width half maximum (FWHM) in cm^{-1} [39].

The experimental nascent OH linewidth also includes contributions from the parent thermal linewidth ($\Delta\nu_{PAAtherm}$) and the probe laser linewidth ($\Delta\nu_{probe}$). The probe linewidth was determined by thermalizing OH products from 266 nm PAA photolysis with 1 Torr of Ar gas, which gave a Gaussian linewidth $\Delta\nu_{exptherm} = 0.209\,cm^{-1}$ FWHM. The experimental thermalized linewidth includes contributions from the OH thermal linewidth, $\Delta\nu_{OHtherm} = 0.0977\,cm^{-1}$ FWHM, and the probe laser linewidth, $\Delta\nu_{probe}$. The probe laser linewidth, $\Delta\nu_{probe} = 0.186\,cm^{-1}$ FWHM, was determined from Eq. (2).

$$(\Delta\nu_{exptherm})^2 = (\Delta\nu_{OHtherm})^2 + (\Delta\nu_{probe})^2 \quad (2)$$

The nascent OH linewidth, $\Delta\nu_{OHnas}$, is then determined from the nascent experimental linewidth in a similar manner where $(\Delta\nu_{expnas})^2 = (\Delta\nu_{OHnas})^2 + (\Delta\nu_{PAAtherm})^2 + (\Delta\nu_{probe})^2$.

The average OH fragment speed, v_{avg}(OH), was determined from $\Delta\nu_{OHnas}$ according to Eq. (3), where c is the speed of light and ν_0 is the line center transition frequency ($R_2 8 = 32591.337\,cm^{-1}$). The values for v_{avg}(OH) are used in the conservation of linear momentum calculations to determine the total average translational energy, E_{tr}(total), of products for reaction pathways (R1–R3).

$$v_{avg}(OH) = \left(\frac{c^2(\Delta\nu_{OHnas})^2}{\pi\,\mathrm{Ln}(2)\nu_0^2}\right)^{1/2} \quad (3)$$

4. Results

Fig. 3 shows the LIF spectrum of OH from photodissociation of PAA at 266 nm. The spectrum was obtained using a fast scan program where some portions of baseline were not collected between spectral transitions in order to speed data collection times. OH radical R_1, R_2, Q_1, and Q_2-branch data were all collected to gather the complete $^2\Pi$ state population distribution. The spectrum was collected using counter-propagating beams and the integrated line intensities showed no particular polarization dependence.

The relative OH rotational state populations were determined by dividing the area of each transition by its Einstein B-factor [40] and the laser intensities. The OH rotational population distributions, spin-orbit ratios, and Λ-doublet ratios at each photolysis wavelength were all determined from the R and Q-branch population data.

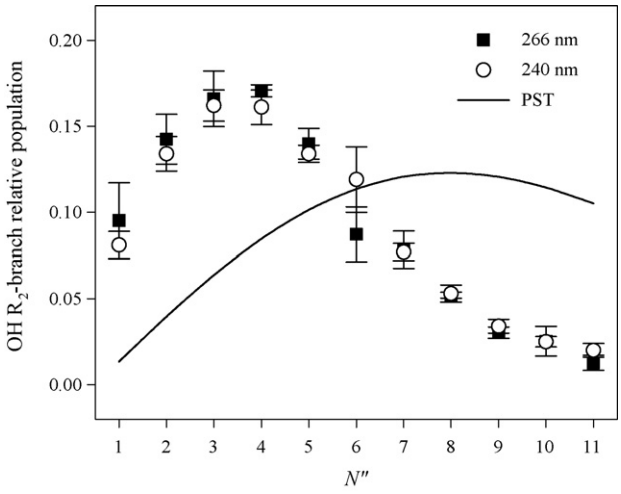

Fig. 4. OH R_2-branch rotational distributions from PAA dissociation at 266 and 240 nm. The distributions, which peak at $N'' \approx 3$–4 and extend to $N'' = 11$, are nearly identical at both photolysis wavelengths. Also included are results from a statistical PST calculation.

The OH $X\,^2\Pi$ ($v'' = 0$) R_2 rotational branch distributions from 266 and 240 nm PAA dissociation are shown in Fig. 4. The R_2 distributions peak around $N'' \approx 3$–4 and extend to $N'' = 11$ and are well fit with Boltzmann distributions. All OH products were produced at the $v'' = 0$ level as there was no measurable signal at $v'' = 1$. Also shown in Fig. 4 are results from a statistical model using a phase-space approach for stepwise O–O dissociation. Phase space theory (PST) assumes a loose transition state and relies upon conservation of energy and angular momentum [41–44]. The PST calculation largely overestimates the experimental OH rotational distribution. PST also indicates a small degree of vibrational excitation that was not seen in our experiments.

Boltzmann plots of the experimental data from all four main branch rotational population distributions were used to calculate the average OH rotational energies and rotational temperatures in Table 1. At both photolysis wavelengths the average OH rotational energies and temperatures are indistinguishable from one another.

The OH $X\,^2\Pi$ ground state spin-orbit population ratios (f_1/f_2) at each excitation wavelength are plotted in Fig. 5. The f_1/f_2 ratios were determined from R_1/R_2 and Q_1/Q_2 average population ratios and are scaled by the m_J state degeneracy $[N''/(N''+1)]$. The average scaled ratios are 1.14 ± 0.18 at 266 nm and 1.16 ± 0.12 at 240 nm, which are both within the

Table 1
Average OH product rotational energies and temperatures after 266 and 240 nm PAA dissociation

Photolysis λ (nm)	Rotational energy (kcal mol^{-1})	T_{rot}(OH) (K)
266	1.47 ± 0.16	742 ± 57
240	1.51 ± 0.13	748 ± 66

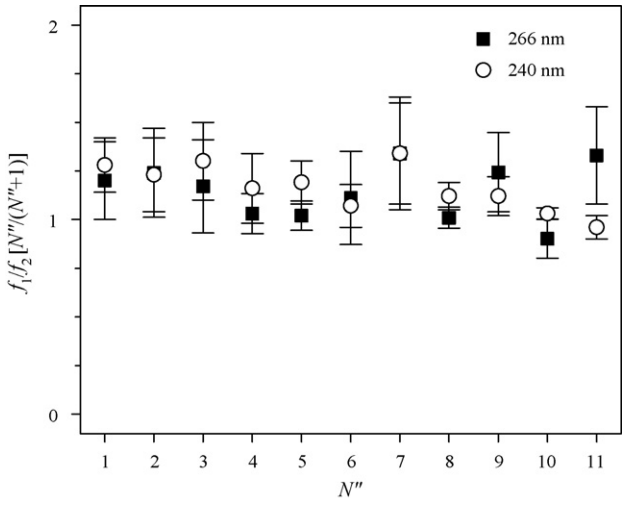

Fig. 5. Ratios of OH $f_1(^2\Pi_{3/2})$ and $f_2(^2\Pi_{1/2})$ spin-orbit split population ratios scaled by the $[N''/(N''+1)]$ state degeneracy after photolysis of PAA at 266 and 240 nm.

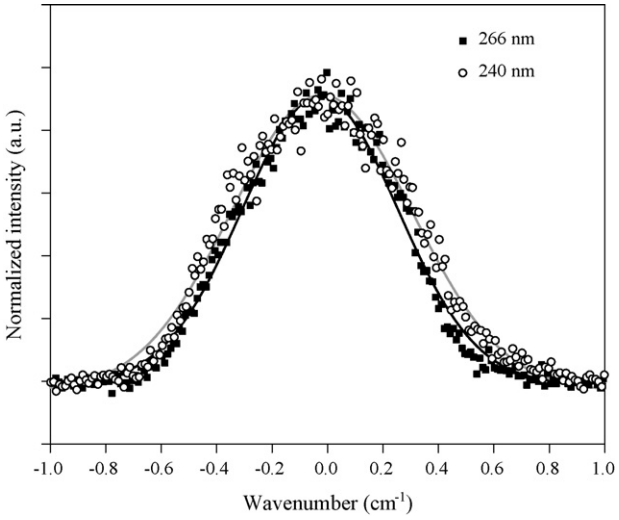

Fig. 7. Experimental Doppler profiles of the OH $R_2 8$ transition after PAA dissociation at 266 and 240 nm shown with Gaussian functions with linewidths $\Delta\nu_{expnas} = 0.68$ and $0.77\,cm^{-1}$ FWHM, respectively.

statistical value near unity but the trend suggests that formation of the f_1 state is slightly preferred.

The OH Λ-doublet ratios (A'/A'') for $N'' \geq 4$ after 266 and 240 nm PAA excitation are shown in Fig. 6. Λ-doublet population ratios indicate whether OH is produced with its single electron occupied p-orbital nominally aligned parallel or perpendicular to the plane of molecular rotation. An A'/A'' ratio of 2/1 indicates a statistical distribution of the Λ-doublet population [45,46]. The average Λ-doublet ratio after 266 nm photolysis is 1.07 ± 0.14, which indicates a preference to generate the A'' state with its lone p-orbital pointing perpendicular to the plane of rotation. This indicates that torsional forces are at work in the dissociation mechanism. The Λ-doublet ratios after 266 nm PAA photolysis increase only slightly with rotation with a ratio of 1.29 ± 0.26 for $N'' = 11$. At 240 nm photolysis, the Λ-doublet ratio increases more dramatically with a ratio of 2.19 ± 0.38 at $N'' = 11$.

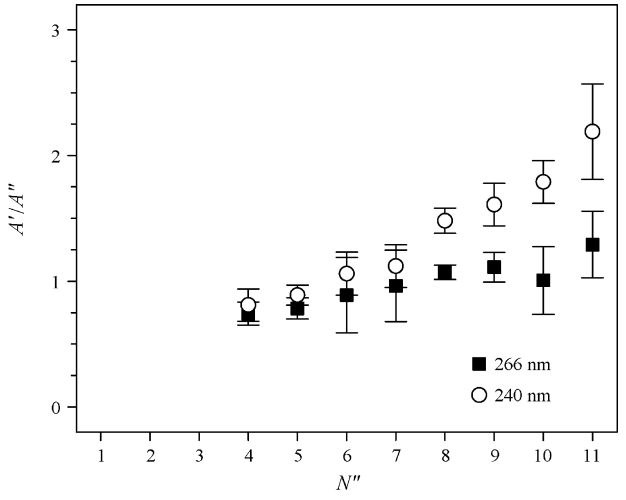

Fig. 6. Λ-doublet ratios of OH A' and A'' states generated from PAA dissociation at 266 and 240 nm were obtained from R_1/Q_1 and R_2/Q_2 average population ratios.

Doppler profiles were obtained for many of the R and Q-branch OH transition lines. The $R_2 8$ lines after 266 and 240 nm PAA photolysis appear in Fig. 7. The average OH translational energies were determined from the linewidth of the Gaussian-fit profiles. The experimental nascent Gaussian-fit linewidth is $\Delta\nu_{expnas} = 0.68\,cm^{-1}$ FWHM for the OH $R_2 8$ line after PAA dissociation at 266 nm.

Gaussian linewidth contributions from the probe laser ($\Delta\nu_{probe} = 0.186\,cm^{-1}$ FWHM) and the thermal velocity of PAA ($\Delta\nu_{PAAtherm} = 0.046\,cm^{-1}$ FWHM) were removed from the experimental nascent linewidths. The deconvoluted nascent OH product linewidth at 266 nm photolysis was $\Delta\nu_{OHnas} = 0.66\,cm^{-1}$ FWHM, which gives an average speed $v_{avg}(OH) = 4100\,m\,s^{-1}$ and an average OH translational energy $E_{tr}(OH) = 34 \pm 2$ kcal mol^{-1}. At 240 nm PAA photolysis the experimental nascent linewidth is $0.76\,cm^{-1}$ FWHM and the deconvoluted nascent OH linewidth is $\Delta\nu_{OHnas} = 0.74\,cm^{-1}$ FWHM with $v_{avg}(OH) = 4600\,m\,s^{-1}$ and $E_{tr}(OH) = 43 \pm 2$ kcal mol^{-1}. The OH translational energies, speeds, and the corresponding translational temperatures after 266 and 240 nm PAA photolysis are summarized in Table 2. There is an increase of 9 kcal mol^{-1} in $E_{tr}(OH)$ when the excitation wavelength is decreased from 266 to 240 nm.

Although a rigorous rotational alignment study was not undertaken in this work, we did observe evidence supporting a degree of OH product vector correlation. Specifically we

Table 2
Nascent OH linewidths $\Delta\nu_{OHnas}$ (FWHM after deconvolution of probe laser and parent PAA linewidths), average speeds $v_{avg}(OH)$, average OH translational energies $E_{tr}(OH)$, and translational temperatures $T_{tr}(OH)$ after 266 and 240 nm excitation

Photolysis λ (nm)	$\Delta\nu_{OHnas}$ (cm^{-1})	$v_{avg}(OH)$ (m s^{-1})	$E_{tr}(OH)$ (kcal mol^{-1})	$T_{tr}(OH)$ (K)
266	0.66	4100	34 ± 2	13 500
240	0.74	4600	43 ± 2	17 000

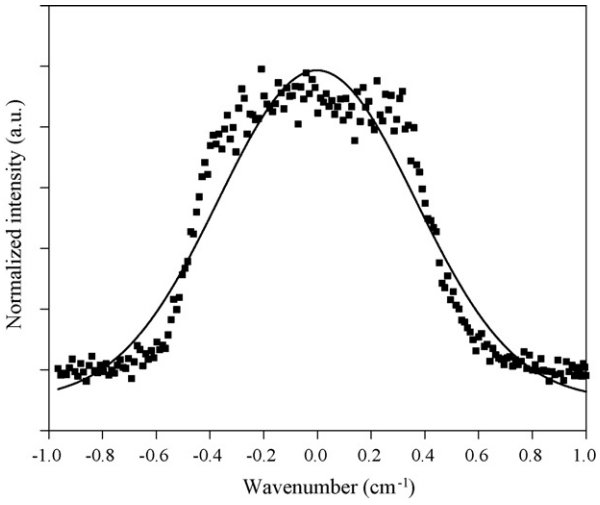

Fig. 8. Experimental Doppler profile of the OH $R_2 1$ transition after 266 nm PAA dissociation shown with a Gaussian function of 0.87 cm^{-1} FWHM. The profile shows evidence for a **v**,**J** vector correlation.

observed an anisotropy in the lineshape of the OH Doppler profiles that is dependent upon the OH rotational level. Lower level rotational transitions, where $N'' = 1$–4, have the strongest degree of anisotropy, but this begins to disappear between $N'' = 5$–7. At $N'' > 7$, the profiles become completely isotropic and are well approximated with Gaussian functions. Fig. 8 shows the OH $R_2 1$ transition after 266 nm photolysis of PAA, which is obviously not fit by a Gaussian function. Vector correlations have been measured in the hydroperoxides, e.g. H_2O_2 [47], CH_3OOH [48], and $(CH_3)_3COOH$ [49]. These peroxides show positive **v**,**J** correlations. This study of PAA photodissociation is focused on discovering the main reaction pathway but a future study is planned to understand the rotational anisotropy. An OH vector correlation study will reveal more specific dynamical information for the dissociation pathway in peroxyacetic acid. The intramolecular hydrogen bond in PAA will probably influence the vector correlations.

5. Discussion

5.1. Total energy analysis of reaction pathways

The reaction pathways (R1–R3) are tested by comparing the total calculated translational energy content of photofragments to the thermochemistry of PAA. The average speed v_{avg}(OH) from experiment is used to determine the total translational energies E_{tr}(total) for the reaction pathways. A pathway is not considered viable if E_{tr}(total) exceeds the thermochemical E_{avail}.

After 266 nm PAA photolysis, OH was produced solely within the ground $^2\Pi$ electronic state at the $v'' = 0$ vibrational level with an average rotational energy of 1.5 kcal mol^{-1} and an average translational energy $E_{tr}(OH) = 34 \pm 2$ kcal mol^{-1}. The internal excitation of OH after 240 nm photolysis is similar to 266 nm results but the broader linewidth of the Doppler profile indicates a 9 kcal mol^{-1} increase in E_{tr}(OH) to 43 ± 2 kcal mol^{-1}. The average speeds of OH are $v_{avg}(OH) = 4100$ m s^{-1} and 4600 m s^{-1} at 266 and 240 nm PAA photolysis,

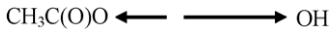

Fig. 9. Linear momentum is conserved between OH and CH_3CO_2 fragments after stepwise O–O dissociation (R1) of PAA. The average OH velocities from experiment are $v_{avg}(OH) = 4100$ and 4600 m s^{-1} after 266 and 240 nm photolysis, respectively. Linear momentum yields 1180 and 1325 m s^{-1} for the acetyloxy average velocities at 266 and 240 nm. E_{tr}(total) = 44 and 55.4 kcal mol^{-1} for the two products at 266 and 240 nm photolysis, which are both below the E_{avail} for this pathway.

respectively. These velocities are used in the following energy analysis of reactions (R1–R3) by applying conservation of linear momentum to the other reaction products in various limiting case dissociation geometries.

5.1.1. Stepwise O–O bond homolysis

In reaction R1 following stepwise O–O dissociation, linear momentum is conserved between $CH_3C(O)O$ and OH. An average speed of 1180 m s^{-1} is calculated for the acetyloxy fragment in Fig. 9 according to Eq. (4).

$$m(CH_3C(O)O)\ v(CH_3C(O)O) = m(OH)\ v_{avg}(OH) \quad (4)$$

The product translational energies, $E_{tr}(CH_3C(O)O) = 10$ kcal mol^{-1} and $E_{tr}(OH) = 34$ kcal mol^{-1}, give E_{tr}(total) = 44 kcal mol^{-1}, which is below the $E_{avail} = 65$ kcal mol^{-1} for stepwise O–O dissociation after 266 nm PAA photolysis (Fig. 1). 240 nm dissociation has $v_{avg}(OH) = 4600$ m s^{-1} and gives $E_{tr}(OH) = 43$ kcal mol^{-1} and $E_{tr}(CH_3C(O)O) = 12.4$ kcal mol^{-1} with E_{tr}(total) = 55.4 kcal mol^{-1}. The thermochemical $E_{avail} = 76.7$ kcal mol^{-1}, which indicates that this pathway is still energetically accessible. Furthermore, subtracting out 3.9 kcal mol^{-1} for the $R_2 8$ OH rotational energy leaves 17.1 and 19.8 kcal mol^{-1} in internal energy of $CH_3C(O)O$ after 266 and 240 nm dissociation, respectively. The extrapolated activation energy for decarboxylation of the acetyloxy radical [50] is 6.6 kcal mol^{-1} and the estimated activation energy for HC(O)O dissociation [51] is 16 kcal mol^{-1}. It is likely that there is enough energy for secondary decarboxylation of the acetyloxy radical.

5.1.2. Concerted C–C and O–O bond dissociation

The concerted pathway (R2), involving simultaneous breakage of O–O and C–C bonds, has three photoproducts with $E_{avail} = 77.2$ and 88.9 kcal mol^{-1} at 266 and 240 nm photolysis, respectively (Fig. 1). The E_{tr}(total) of the three products was calculated through conservation of linear momentum using the experimental average OH velocities. Consideration of the PAA molecular geometry was used in the calculations in a manner similar to acetic acid [23,24]. For acetic acid a C–C–O bond angle of 109° was assumed because the $n \rightarrow \pi^*$ transition results in a planar to pyramidal change at the carbonyl carbon. For PAA, absorption likely occurs through an $n \rightarrow \sigma^*$ transition on the peroxy chromophore and the geometry at the carbonyl carbon is not expected to change. The following calculations assume that the planar conformation of PAA is conserved in the excited electronic state. The first geometry or case (a) *simple concerted* in Fig. 10 has all three photofragments departing from one another symmetrically at equal angles ($\theta = 120°$) within the molecular

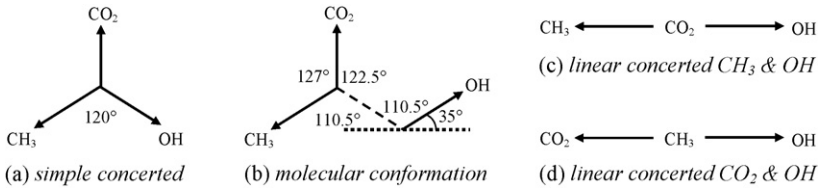

Fig. 10. Diagram for concerted dissociation of PAA. The experimental $v_{avg}(OH) = 4100$ and 4600 m s^{-1} at 266 and 240 nm and the calculated values for $v(CH_3)$ and $v(CO_2)$ in the following cases are given sequentially for 266 and 240 nm dissociation. For case (a) *simple concerted*, $v(CH_3) = 4650$ and 5210 m s^{-1} and $v(CO_2) = 1580$ and 1780 m s^{-1}. E_{tr}(total) = 86.1 and 108.2 kcal mol^{-1} at 266 and 240 nm, both higher than the E_{avail}. In case (b) *molecular conformation*, the ab initio geometry of PAA is used. The velocities are $v(CH_3) = 4660$ and 5220 m s^{-1} and $v(CO_2) = 0$ m s^{-1} at both wavelengths. E_{tr}(total) = 73.1 and 91.8 kcal mol^{-1} at 266 and 240 nm, each very near the E_{avail}. The case (c) *linear concerted CH3 and OH* scenario where CO_2 is stationary gives results similar to the case (b) calculations with $v(CH_3) = 4650$ and 5210 m s^{-1} and E_{tr}(total) = 72.9 and 91.7 kcal mol^{-1}. The case (d) *linear concerted CO2 and OH* calculation where CH_3 remains stationary gives $v(CO_2) = 1580$ and 1780 m s^{-1} and E_{tr}(total) = 47.4 and 59.6 kcal mol^{-1}.

plane. Momentum is conserved between OH and the two other fragments in the vertical and horizontal directions of the molecular plane according to Eqs. (5) and (6) where $\alpha,\beta = \theta/2$. After 266 nm dissociation E_{tr}(total) is 86.1 kcal mol^{-1}, which is substantially higher than the E_{avail} of 77.2 kcal mol^{-1}. After 240 nm photolysis, the three products have E_{tr}(total) = 108.2 kcal mol^{-1}, which is also greater than E_{avail} = 88.9 kcal mol^{-1}. Case (a) *simple concerted* can be eliminated because the calculated translational energies are higher than the E_{avail} for the pathway.

$$m(CO_2)v(CO_2) = m(CH_3)\ v(CH_3)\ \cos\alpha + m(OH)\ v_{avg}(OH)\ \cos\beta \quad (5)$$

$$m(CH_3)v(CH_3)\sin\alpha = m(OH)\ v(OH)\ \sin\beta \quad (6)$$

Another case for concerted dissociation utilizes the *molecular conformation* of PAA [7,8] to calculate E_{tr}(total). The geometry shown in case (b) uses a C–C=O bond angle of 127° and a C–O–O bond angle of 110.5°. The center of dissociation is still the same as in Fig. 10 case (a). To perform the calculation the OH velocity vector is moved to the dissociation center along the dashed line so all three product velocity vectors originate from the same point. E_{tr}(total) determined from Eqs. (5) and (6), where $\alpha = 55.25°$ and $\beta = 90° + 35° = 125°$, is 73.1 kcal mol^{-1} at 266 nm, which is 95% of the E_{avail} = 77.2 kcal mol^{-1}. At 240 nm, E_{tr}(total) of all three fragments is 91.8 kcal mol^{-1}, which is slightly higher than E_{avail} = 88.9 kcal mol^{-1}.

Similar to case (b) is the case (c) *linear concerted CH3 and OH* pathway. In case (c) momentum is partitioned linearly between OH and CH_3, which leaves CO_2 stationary. For case (c) E_{tr}(total) = 72.9 and 91.7 kcal mol^{-1} at 266 and 240 nm and like case (b) the E_{tr}(total) values are very near the concerted pathway available energies.

Another possibility for concerted linear dissociation is case (d) where linear momentum is shared between OH and CO_2, and CH_3 remains stationary. E_{tr}(total) of products for this scenario at 266 nm photolysis is 47.4 kcal mol^{-1}, which is within the E_{avail} = 77.2 kcal mol^{-1}. At 240 nm E_{tr}(total) = 59.6 kcal mol^{-1} where E_{avail} = 88.9 kcal mol^{-1}. Case (d) cannot be ruled out as it is energetically possible but such a scenario is unlikely for a concerted reaction because substantial molecular rearrangement is necessary to channel so much kinetic energy into the CO_2 product. It is more likely that two relatively equal and opposing forces would be applied to CO_2 during simultaneous bond breaking in PAA more like case (c).

5.1.3. Stepwise C–C bond homolysis

The second stepwise pathway beginning with C–C bond cleavage (R3) has E_{avail} = 77.2 and 88.9 kcal mol^{-1} after 266 and 240 nm photolysis but produces OH only after secondary C(O)OOH decomposition. Two cases for dissociation along this pathway are shown in Fig. 11. Case (I) considers the possibility that all E_{tr}(OH) comes from C–C bond breaking. The E_{avail} after initial C–C bond homolysis are 13.5 and 25.2 kcal mol^{-1} at 266 and 240 nm photolysis, respectively (see Fig. 1). Homolysis of the C–C bond in case (I) is insufficient to produce OH in the form of C(O)OOH product translation with the E_{tr}(OH) values measured in these experiments. In case (II), all E_{tr}(OH) comes from secondary O–O fission of C(O)OOH, which imparts 63.7 kcal mol^{-1} of available energy to OH and CO_2 regardless of the photolysis energy. The calculated E_{tr}(total) of OH and CO_2 in case (II) after 266 nm photolysis is 47 kcal mol^{-1} (34 and 13 kcal mol^{-1} for OH and CO_2 respectively), which is below the E_{avail} from secondary dissociation. The calculated E_{tr}(total) after 240 nm photolysis is 59.6 kcal mol^{-1} (43 and 16.6 kcal mol^{-1} for OH and CO_2), which is very near the E_{avail} (still 63.7 kcal mol^{-1}). Because E_{tr}(OH) from experiment increases significantly from 266 to 240 nm PAA photolysis and the high calculated E_{tr}(total) at 240 nm compared to the E_{avail} (59.6 compared to 63.7 kcal mol^{-1}) are both indications that case

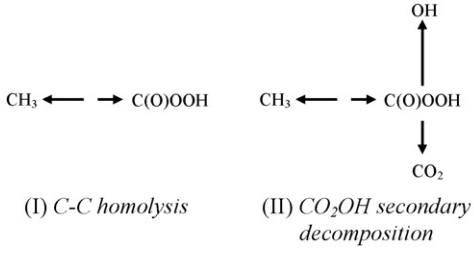

Fig. 11. Conservation of linear momentum for stepwise C–C dissociation (R3) of PAA. Case (I) *C–C homolysis* of PAA gives CH_3 and C(O)OOH fragments but the E_{avail} after 266 and 240 nm excitation, 13.5 and 25.2 kcal mol^{-1}, are insufficient to produce OH at the experimental velocities. In case (II) *C(O)OOH secondary decomposition* produces OH and CO_2 with $v(CO_2) =$ 1580 and 1780 m s^{-1}. Case (II) is energetically allowable but several arguments can be made to limit it as an unlikely pathway.

(II) is not followed. It is unlikely that a secondary decomposition process would generate such high OH product velocities. Also, the O–O bond is the weakest in PAA at 42.5 kcal mol^{-1} while the C–C bond is estimated to be 94 kcal mol^{-1}. UV absorbance in PAA occurs in the peroxy chromophore so it seems highly unlikely that energy could be so easily transferred to break a much stronger bond.

5.1.4. Other possible pathway considerations

Another pathway for PAA not shown in Fig. 1 involves C–O single bond cleavage resulting in $CH_3C(O) + OOH$. This pathway also requires a large amount of energy for bond breaking, 80 kcal mol^{-1} according to group-additivity methods or 84 kcal mol^{-1} based upon MO ab initio calculations [10]. This leaves only 23.5–26.3 kcal mol^{-1} of available energy. Secondary decomposition of OOH through O–O bond dissociation requires 68.3 kcal mol^{-1} to form $O(^3P) + OH(X^2\Pi)$ on the ground state potential surface [52]. This pathway is not a likely source of OH production from PAA dissociation.

5.2. Review of UV absorption spectra of PAA, acetic acid, H_2O_2, and MHP

To get a better understanding of the dissociation process of PAA it is worthwhile to discuss its absorbing chromophores and compare to other similar molecules. PAA contains both peroxy and carbonyl chromophores. The absorption spectra of PAA, acetic acid, H_2O_2, and methylhydroperoxide (MHP) are shown in Fig. 12. The UV spectrum of PAA in solution was measured some time ago and is similar to H_2O_2 but with somewhat reduced extinction [53]. The spectra of gas phase PAA and acetic acid monomer were measured recently [54]. The spectrum of acetic acid monomer begins at 244 nm. A previous vapor phase absorbance measurement of acetic acid, assuming monomer only but likely having dimer contribution, had $\lambda_{max} = 203$ nm for the $n \rightarrow \pi^*$ ($S_0 \rightarrow S_1$) band [55]. The spectra of H_2O_2 and MHP both have a rising continuum from 340 to 210 nm [56]. MHP is reduced in absorption cross section relative to H_2O_2 at each wavelength. H_2O_2 and MHP both absorb in the UV via $n \rightarrow \sigma^*$ transitions in the peroxy group. The spectrum of PAA is reduced in cross section relative to MHP in the long wavelength tail. At around 228 nm the spectrum of PAA increases in cross section above MHP, which continues to 210 nm. The increased absorbance of PAA above MHP at shorter wavelengths is possibly due to additional absorption from the carbonyl chromophore.

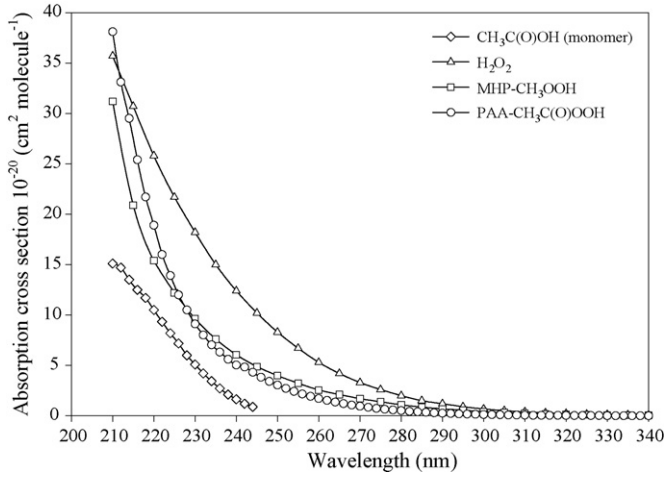

Fig. 12. Gas phase UV absorption spectra of PAA-$CH_3C(O)OOH$ (circles), acetic acid monomer-$CH_3C(O)OH$ (diamonds), H_2O_2 (triangles), and MHP-CH_3OOH (squares) [54,56].

It is important to address the electronic transitions that occur at each excitation wavelength in these experiments because the dissociation dynamics are likely to change if different electronic manifolds are accessed. PAA absorption from 340 to 244 nm is due solely to a peroxy $n \rightarrow \sigma^*$ transition but below 244 nm there may be additional absorbance from a carbonyl $n \rightarrow \pi^*$ transition. At 266 nm PAA absorbs specifically by a peroxy $n \rightarrow \sigma^*$ transition similar to H_2O_2 and MHP. The absorption cross section for PAA is higher at 240 nm than at 266 nm (5.03 and 1.21×10^{-20} cm^2 molecule^{-1}, respectively). As indicated by the spectrum of acetic acid, some of the absorption by PAA at 240 nm may be from the carbonyl chromophore. At 240 nm the absorption cross section for acetic acid is 1.64×10^{-20} cm^2 molecule^{-1} and the estimated maximum ratio of peroxy to carbonyl absorption in PAA would be about 3 to 1. This suggests most of the OH signal measured from PAA at 240 nm is still due to peroxy absorption.

5.3. Direct versus indirect dissociation

Dissociation from either a repulsive excited electronic state or from a predissociative bound state with a large exit channel barrier is expected for PAA because OH is produced with a large amount of translational energy. The difference in excitation energy between 266 and 240 nm photolysis (11.6 kcal mol^{-1}) becomes added available energy to the reaction pathways, which provides a means to determine the direct versus indirect nature of the dissociation process and the type of electronic transition accessed by PAA. If the mechanism is directly dissociative, an increase in the average E_{tr}(OH) at the higher photolysis energy is expected and the fraction of E_{avail} imparted into translation would be similar at both excitation wavelengths. If dissociation is indirect, the average E_{tr}(OH) should be nearly the same at both photolysis wavelengths and the percentage of E_{avail} partitioned to translation should decrease at the higher photolysis energy.

The stepwise O–O pathway (R1) is most likely for PAA and is therefore the only pathway considered in the direct versus indirect mechanism analysis. Table 3 lists the photolysis wave-

Table 3
Energy partitioning into OH and $CH_3C(O)O$ products along the stepwise O–O pathway (R1) from PAA photolysis at 266 and 240 nm (all energies are in kcal mol^{-1})

Photolysis λ (nm)	Photolysis energy	E_{avail}	E_{int}(OH), % of E_{avail}	E_{tr}(OH)	E_{tr}(total), % of E_{avail}
266	107.5	65.0	1.5, 2.3%	34.0	44.0, 67.7%
240	119.2	76.7	1.5, 2.0%	43.0	55.4, 72.2%

lengths and energies, the E_{avail} for the stepwise O–O pathway, E_{int}(OH) the average OH internal energy, E_{tr}(OH) the average OH translational energy, and E_{tr}(total) the calculated total translational energy. The percentage of E_{avail} partitioned into E_{int}(OH) and E_{tr}(total) is also listed. The average OH rotational energy is 1.5 kcal mol^{-1} for both photolysis wavelengths and the portion of E_{avail} going into OH rotation decreases slightly at the higher photolysis energy. The average E_{tr}(OH) increases from 34 to 43 kcal mol^{-1} between 266 and 240 nm photolysis. The E_{tr}(total) of the two stepwise products increases from 44 to 55.4 kcal mol^{-1} from 266 to 240 nm excitation. The percentages of E_{avail} going into E_{tr}(total) are 67.7% at 266 nm and 72.2% at 240 nm photolysis. Perhaps not coincidently, the increase in E_{tr}(total) of 11.4 kcal mol^{-1} for the stepwise O–O pathway is nearly equal to the 11.6 kcal mol^{-1} of increased E_{avail} provided by increasing the photolysis energy. The increases in E_{tr}(OH) and E_{tr}(total) and the nearly identical OH rotational distributions between 266 and 240 nm indicate the dissociation process is likely direct from a repulsive excited state. The nearly similar but slightly increasing percentages of E_{avail} partitioned into E_{tr}(total) between the 266 and 240 nm studies confirms the process is direct. An indirect mechanism would produce nearly equal amounts of E_{tr}(OH) and E_{tr}(total) at both excitation wavelengths, and the partitioning of energy into translation would decrease.

5.4. Comparison of PAA photodissociation results to carboxylic acid and peroxide studies

The first $n \rightarrow \pi^*$ electronic transition in formic acid excites vibronic bands in carbonyl stretching and O–C–O bending motions as well as C–H out of plane and O–H torsional motions [57]. Formic acid photolysis studied at 225 nm places 78% of the available energy into translation of HCO and OH and the remaining energy into HCO internal excitation and OH was produced in the ground electronic state with no vibrational and only a small amount of rotational energy [58]. The high partitioning of energy into translation was indicative of a high exit barrier that appeared to be insensitive to vibronic state selection [59].

Photodissociation of acetic acid from the $^1(n,\pi^*)$ state is stepwise starting with C–O bond fission where OH was produced in the ground electronic state over an exit channel barrier after $S_1 \rightarrow T_1$ intersystem crossing [23,24]. Secondary decomposition of CH_3CO to produce $CH_3 + CO$ was possible at 200 nm. After 218 nm photolysis of acetic acid, CH_3CO and OH products were generated with a large amount of translational energy (49% of the available) and OH was produced with little rotational (4%) and no vibrational energy [23]. After 200 nm acetic acid dissociation, the energy partitioning was 36% in total translation and 3.4% in OH rotation [24]. The remaining available energy in both experiments was deposited into internal excitation of the acetyl fragment. Photodissociation of acetic acid at 193 nm produces OH with nearly the same translational energy as 218 and 200 nm photolysis [60]. The exit channel barrier with a height around 14 kcal mol^{-1} and attributed to the T_1 surface similar to acetone [25,61], was the likely source for translational energy production.

H_2O_2 photodissociation has been studied at many UV wavelengths. At 266 nm OH products were generated with 90% of the energy available in translation [47]. The remaining available energy went into OH rotation, which had no measurable vibrational energy. The long wavelength tail of the H_2O_2 spectrum corresponds to $n \rightarrow \sigma^*$ absorption and electron promotion from the $X\,^1A$ ground state to the A^1A repulsive excited state. Doppler and polarization spectroscopy of OH fragments showed that the repulsive A^1A excited electronic state of H_2O_2 is exclusively accessed at 266 nm.

Methyl hydroperoxide (MHP, CH_3OOH) photolyzed in a molecular beam at 193 and 248 nm produced $CH_3O + OH$ exclusively at both wavelengths [62]. The average translational energy of the two photofragments was 65% and 67% of the available energy at 193 and 248 nm, respectively. The bulk of the remaining available energy was imparted into internal excitation of the CH_3O fragment. The large product translational energies and similar energy partitioning at each photolysis wavelength indicated that dissociation was direct from a highly repulsive potential energy surface. Energy partitioning of MHP photofragments after 266 nm excitation was similar [48].

Photodissociation of *tert*-butyl hydroperoxide at 248 nm produced *t*-BuO and OH with 60% of the available energy partitioned into translation of the products, 5% in OH rotation, and the remainder in *t*-BuO internal excitation [49]. The dissociation process was also consistent with a directly-dissociative repulsive excited electronic state.

The increase in molecular complexity from H_2O_2 to larger alkyl hydroperoxides puts more of the available energy into the internal degrees of freedom of the larger photofragment but OH is still produced with very high translational energies. All the hydroperoxides show evidence of direct dissociation from repulsive surfaces after UV excitation in the long wavelength tail of the absorption continuum. The percent of E_{avail} partitioned into translation of $CH_3C(O)O$ and OH after 266 nm PAA photolysis (67.7% from Table 3) is similar to the translational energy partitioning (67%) into CH_3O and OH after 248 nm MHP dissociation. It is reasonable to conclude that PAA undergoes UV photodissociation in a manner similar to the hydroperoxides based upon the likelihood of the stepwise O–O reaction and the evidence for direct dissociation.

6. Conclusions

The dominant photodissociation pathway of PAA at 266 and 240 nm excitation results in $CH_3C(O)O$ and OH photofragments through reaction R1, the stepwise pathway initiated by O–O bond breaking, which is likely followed by secondary acetyloxy radical decomposition. The concerted reaction R2 with simultaneous O–O and C–C bond dissociation is not likely based on our analysis. The only energetically feasible analysis of the concerted pathway is in Fig. 10 case (d) where all of the momentum opposite of OH is applied to CO_2, but this case seems highly unlikely in terms of the molecular geometry of PAA. A second stepwise reaction (R3), beginning with C–C bond dissociation also cannot be entirely eliminated as a possible minor pathway as there are no energetic constraints but is expected to be

very unlikely because a large fraction of the excitation energy is needed to cleave the C–C bond.

A comparison of experimental OH energy distributions to those calculated by a statistical model for stepwise O–O bond dissociation indicate that the reaction shows effects of excited state dissociation. A comparison of the OH product energy content after 266 and 240 nm photolysis provides strong evidence for direct dissociation likely from a repulsive electronic state. The increase in the average E_{tr}(OH) and the similar translational energy partitioning at both photolysis wavelengths lead to the direct mechanism. This argument was made using the average translational energy of OH, which actually consists of a distribution of velocities. Analysis of slower translational products may lead to discovery of minor dissociation pathways.

Absorption of PAA at both 266 and 240 nm is largely due to an $n \rightarrow \sigma^*$ transition on the peroxy chromophore. The direct nature of the stepwise O–O dissociation pathway indicates that the mechanism in PAA is similar to H_2O_2 and the alkyl hydroperoxides. PAA does not absorb by the $n \rightarrow \pi^*$ carbonyl transition at the wavelengths studied here and does not follow indirect dissociation over a barrier like formic and acetic acid. At wavelengths shorter than 240 nm, PAA may have some carbonyl absorption and dissociation may proceed like acetic acid but the results would likely be drowned out by dissociation from peroxy bond excitation due to its larger absorption cross section.

To further understand the photodissociation process of peroxy acids as a group, it will prove useful to investigate other peroxy acid compounds. Peroxybenzoic and phenylperoxy acetic acid are two other interesting aromatic peroxy acids planned for study. Peroxybenzoic acid should generate a highly unstable phenyl radical in the concerted reaction, which eliminates the favorable thermochemistry for this pathway. Phenylperoxyacetic acid, on the other hand, produces a very stable benzyl radical, which increases the available energy in the concerted pathway. This will test whether favorable thermochemistry may drive dissociation towards the concerted pathway and will also test whether adjusting the stability of the R radical can influence the dissociation pathway branching ratio to favor one mechanism over the other as has been suggested in thermal decomposition studies of peroxy esters. Changing the relative available energy between stepwise and concerted pathways by changing the R group in the molecule may effectively change the branching ratio between the reaction pathways unless photodissociation is again determined by electronic excited states. Increasing the molecular complexity of the peroxy acid will also test the degree of non-statistical behavior in the dissociation process. A larger peroxy acid with many more degrees of freedom is more likely to dissociate on the ground state potential surface by a statistical mechanism.

Acknowledgement

The authors would like to thank the Office of Naval Research, Department of Atomic and Molecular Physics (N00014-99-1-0573) for support of this research.

References

[1] P.A. Giguere, A.W. Olmos, Can. J. Chem. 30 (1952) 821.
[2] J. Chao, B.J. Zwolinski, J. Phys. Chem. Ref. Data 7 (1978) 363.
[3] D. Swern, Organic Peroxides, I, Wiley-Interscience, New York, 1970.
[4] A.C. Egerton, W. Emte, G.J. Minkoff, Discuss. Faraday Soc. 10 (1951) 278.
[5] J.R. Rittenhouse, W. Lobunez, D. Swern, J.G. Miller, J. Am. Chem. Soc. 80 (1958) 4850.
[6] M. Oldani, T.-K. Ha, A. Bauder, J. Am. Chem. Soc. 105 (1983) 360.
[7] J.A. Cugley, W. Bossert, A. Bauder, Hs.H. Gunthard, Chem. Phys. 16 (1976) 229.
[8] R. Benassi, F. Taddei, J. Molec. Struct. (Theochem.) 303 (1994) 83.
[9] S.W. Benson, Thermochemical Kinetics, second ed., Wiley-Interscience, New York, 1976.
[10] R. Benassi, F. Taddei, Tetrahedron 50 (1994) 4795.
[11] R. Benassi, F. Taddei, J. Molec. Struct. (Theochem.) 303 (1994) 101.
[12] R.D. Bach, P.Y. Ayala, H.B. Schlegel, J. Am. Chem. Soc. 118 (1996) 12758.
[13] A.J. Colussi, M.A. Grela, Int. J. Chem. Kinet. 30 (1998) 41.
[14] R.C.P. Cubbon, Prog. React. Kinet. 5 (1970) 29.
[15] R.A. Sheldon, J.K. Kochi, J. Am. Chem. Soc. 92 (1970) 5175.
[16] C. Schmidt, A.H. Sehon, Can. J. Chem. 41 (1963) 1819.
[17] F.W. Evans, A.H. Sehon, Can. J. Chem. 41 (1963) 1826.
[18] Y. Ogata, K. Tomizawa, J. Org. Chem. 43 (1978) 261.
[19] Y. Ogata, K. Tomizawa, J. Org. Chem. 44 (1979) 2770.
[20] Y. Ogata, K. Tomizawa, J. Org. Chem. 45 (1978) 785.
[21] Y. Ogata, K. Tomizawa, Bull. Chem. Soc. Jpn. 53 (1980) 2419.
[22] D.L. Heywood, B. Phillips, H.A. Stansburg Jr., J. Org. Chem. 26 (1961) 281.
[23] S.S. Hunnicutt, L.D. Waits, J.A. Guest, J. Phys. Chem. 93 (1989) 5188.
[24] S.S. Hunnicutt, L.D. Waits, J.A. Guest, J. Phys. Chem. 95 (1991) 562.
[25] S.W. North, D.A. Blank, J.D. Gezelter, C.A. Longfellow, Y.T. Lee, J. Chem. Phys. 102 (1995) 4447.
[26] H. Krimm, U.S. Patent 2,813,896 (1957).
[27] F.P. Greenspan, D.G. MacKellar, Anal. Chem. 20 (1948) 1061.
[28] N. Bloembergen, Y.R. Shen, Phys. Rev. Lett. 12 (1964) 504.
[29] V. Wilke, W. Schmidt, Appl. Phys. 18 (1979) 177.
[30] J.F. Córdova, C.T. Rettner, J.L. Kinsey, J. Chem. Phys. 75 (1981) 2742.
[31] R. Altkorn, R.N. Zare, Ann. Rev. Phys. Chem. 35 (1984) 265.
[32] A. Jacobs, M. Wahl, R. Weller, J. Wolfrum, Appl. Phys. B 42 (1987) 173.
[33] J.A. Coxon, Can. J. Phys. 58 (1980) 933.
[34] G.H. Dieke, H.M. Crosswhite, J. Quant. Spectrosc. Radiat. Transfer 2 (1962) 97.
[35] E.A. Moore, W.G. Richards, Phys. Scripta 3 (1971) 223.
[36] M. Nub, K.-H. Gericke, F.J. Comes, J. Quant. Spectrosc. Radiat. Transfer 27 (1982) 191.
[37] P. Houston, Chemical kinetics and reaction dynamics, Mosby-Year Book, Inc, Ithaca, NY, 1995.
[38] G. Herzberg, The Spectra and Structures of Simple Free Radicals, Cornell University Press, New York, 1971.
[39] W. Demtroder, Laser spectroscopy, second Ed., Springer-Verlag, New York, 1998.
[40] I.L. Chidsey, D.R. Crosley, J. Quant. Spectros. Rad. Transfer 23 (1980) 187.
[41] A. Sinha, R.L. Vander Wal, F.F. Crim, J. Chem. Phys. 92 (1990) 401.
[42] P. Pechukas, J.C. Light, J. Chem. Phys. 42 (1965) 3281.
[43] P. Pechukas, J.C. Light, C. Rankin, J. Chem. Phys. 44 (1966) 794.
[44] J.C. Light, Faraday Discuss. Chem. Soc. 44 (1967) 14.
[45] M.J. Bronikowski, R.N. Zare, Chem. Phys. Lett. 166 (1990) 5.
[46] M.D. Wojcik, T.R. Fletcher, J. Chem. Phys. 117 (2002) 1507.
[47] K. Gericke, S. Klee, F.C. Comes, R.N. Dixon, J. Chem. Phys. 85 (1986) 4463.
[48] S.W. Novicki, R. Vasudev, J. Chem. Phys. 93 (1990) 8725.
[49] J. August, M. Brouard, M.P. Docker, A. Hodgson, C.J. Milne, J.P. Simons, R. Lavi, S. Rosenwaks, D. Schwartz-Lavi, J. Phys. Chem. 92 (1988) 5485.
[50] W.J. Braun, L. Rajbenbach, F.R. Eirich, J. Phys. Chem. 66 (1962) 1591.
[51] G.C. Schatz, M.S. Fitzcharles, Faraday Discuss. Chem. Soc. 84 (1987) 359.

[52] W.J. Lemon, W.L. Hase, J. Phys. Chem. 91 (1987) 1596.
[53] P.A. Giguere, A.W. Olmos, Can. J. Chem. 34 (1956) 689.
[54] J.J. Orlando, G.S. Tyndall, J. Photochem. Photobiol. A: Chem. 157 (2003) 161.
[55] J.G. Calvert, J.N. Pitts Jr., Photochemistry, Wiley, New York, 1966.
[56] S.P. Sander, R.R. Friedl, D.M. Golden, M.J. Kurylo, G.K. Moortgat, H. Keller-Rudek, P.H. Wine, A.R. Ravishankara, C.E. Kolb, M.J. Molina, B.J. Finlayson-Pitts, R.E. Huie, V.L. Orkin, Chemical kinetics and photochemical data for use in stratospheric modeling, Evaluation no. 15, NASA JPL Publication 06-02, 2006.
[57] F. Ioannoni, D.C. Moule, D.J. Clouthier, J. Phys. Chem. 94 (1990) 2290.
[58] M. Brouard, J. O'Mahony, Chem. Phys. Lett. 149 (1988) 45.
[59] M. Brouard, J.P. Simons, J.-X. Wang, Faraday Discuss. Chem. Soc. 91 (1991) 63.
[60] H.T. Kwon, S.K. Shin, S.K. Kim, H.L. Kim, C.R. Park, J. Phys. Chem. A 105 (2001) 6775.
[61] L.D. Waits, R.J. Horwitz, J.A. Guest, Chem. Phys. 155 (1991) 149.
[62] M.-A. Thelen, P. Felder, J.R. Huber, Chem. Phys. Lett. 213 (1993) 275.